coatings

MDPI

Article

Modeling of Solid Particle Erosion for a Water–Sand Impingement System Using OpenFOAM

Mateo Narváez [1,2], Cristian Cruzatty [1,2], Esteban Valencia [1,2], Víctor Hidalgo [1,2,3,4], Xianwu Luo [5], Alejandra Torres [1], José Erazo [1,2], Gonzalo Altamirano [6] and Edgar Cando [1,2,7,*]

1 Departamento de Ingeniería Mecánica, Escuela Politécnica Nacional, Quito 170517, Ecuador; mateo.narvaez@epn.edu.ec (M.N.); cristian.cruzatty@epn.edu.ec (C.C.); esteban.valencia@epn.edu.ec (E.V.); victor.hidalgo@epn.edu.ec (V.H.); lisbeth.torres@epn.edu.ec (A.T.); jose.erazo@epn.edu.ec (J.E.)
2 Grupo de Investigación de Aeronáutica y Termofluidos Aplicada, Escuela Politécnica Nacional, Quito 170517, Ecuador
3 Carrera de Pedagogía Técnica de la Mecatrónica, Facultad de Filosofía, Letras y Ciencias de la Educación, Universidad Central del Ecuador, Quito 170129, Ecuador
4 Centro de Investigación en Mecatrónica y Sistemas Interactivos—MIST, Universidad Indoamérica, Av. Machala y Sabanilla, Quito 170103, Ecuador
5 Department of Energy and Power Engineering, Tsinghua University, Beijing 100084, China; luoxw@tsinghua.edu.cn
6 Centro de Investigación y Recuperación de Turbinas Hidráulicas y Partes Industriales, CELEC EP, Baños de Agua Santa 180254, Ecuador; gonzalo.altamirano@celec.gob.ec
7 Escuela de Ingeniería Mecatrónica, Universidad Internacional del Ecuador, Quito 170411, Ecuador
* Correspondence: edgar.cando@epn.edu.ec; Tel.: +593-97-928-8606

Abstract: The development of accurate methodologies for a thorough comprehension of the erosion phenomenon is a challenging and necessary task. This study entailed an exhaustive analysis, incorporating empirical data obtained from an experiment involving the impingement of a sand and water jet on a submerged stainless-steel plate and numerical simulations, employing the Oka Erosion model that was compiled in OpenFOAM. The primary focus of this study was to generate W-shaped profiles delineating the impingement zone, derived both from experimental observations and the developed numerical model. This comparative approach facilitated a robust evaluation of the model's efficacy in replicating erosion patterns. The outcomes of this analysis revealed a concurrence between the experimental and simulated erosion contours, affirming the model's proficiency in representing erosion phenomena. Nevertheless, a minor discrepancy was noted, characterized by a slight underestimation of erosion rate and thickness loss. Furthermore, the investigation unveiled a noteworthy time-dependent trend in mass loss from the experimental data denoting a pseudo stabilization of the erosion rate across the time. This research contributes to the refinement of erosion modeling parameters and underscores the nature of time-dependent erosion behavior, a pivotal consideration for optimizing material durability.

Keywords: erosion model; sediment erosion; jet impingement; material wear analysis; computational erosion analysis; CFD; OpenFOAM

Citation: Narváez, M.; Cruzatty, C.; Valencia, E.; Hidalgo, V.; Luo, X.; Torres, A.; Erazo, J.; Altamirano, G.; Cando, E. Modeling of Solid Particle Erosion for a Water–Sand Impingement System Using OpenFOAM. *Coatings* **2023**, *13*, 2080. https://doi.org/10.3390/coatings13122080

Academic Editors: Giorgos Skordaris and Emerson Coy

Received: 1 August 2023
Revised: 25 October 2023
Accepted: 27 October 2023
Published: 13 December 2023

1. Introduction

To find solutions to the effects of erosion wear, several proposals have been given to improve the surface integrity of steel hydraulic machinery runners [1]. These include superfinishing processes like burnishing [2,3], honing, and grinding [3], and the use of composite coatings such as NI–Al_2O_3, Ni–Al_2O_3–TiO_2 CoNiCrAlY [4] and WC–Co–Cr [5], deposited using different techniques such as High Velocity Air-Fuel (HVAF), Atmospheric plasma spray (APS), and High Velocity Oxygen Fuel (HVOF) [6]. In addition, the necessity for erosion testing and modeling extends beyond the realm of hydropower and has significant implications in various industries. For instance, anti-reflective coatings, such

as those used in photovoltaic glass covers, are vulnerable to degradation by erosion [7,8]. Erosion-induced deterioration of these coatings can result in reduced optical and mechanical properties, impacting their overall performance. Therefore, understanding erosion phenomena and developing accurate predictive models are crucial not only for hydropower applications but also for enhancing the durability and performance of materials in diverse industries.

However, before implementing coating solutions, it is necessary to evaluate the fundamental response of the material to the wear mechanisms to which the workpiece will be subject. In this context, numerous predictive models for estimating erosion have been developed and proposed by several authors, including Finnie, McLurry, Grant Tabackoff, and Arabnejad models [9–12]. These models have successfully served as approximations for various sediment erosion conditions. Between these, some have been settled from the compilation of experimental data and through theoretical formulations from the equations of motion and material removal of the particle [9–11].

Among the array of erosion prediction methods, one particularly robust approach is the Oka erosion model [13,14]. This model was estimated from experimental data by direct sand impact on test specimens of different materials at several particle velocities and impingement angles. Most of the data were obtained from a sandblast type test rig that eroded the specimen located at the end of the nozzle in an air chamber. This erosion model incorporates various factors such as sediment characteristics, flow velocity, and hydraulic parameters to simulate erosion behavior. However, despite its potential, there is a need for further investigation and evaluation of the model's effectiveness in practical scenarios.

The Oka erosion model can be used to estimate the erosion rate caused by particle impingement on the blades and other turbomachinery components. In addition, this can be used to optimize equipment design and operation by predicting equipment life and identifying potential erosion hotspots. This model considers impact parameters such as particle velocity, angle of impingement, and particle size, as well as the material properties of the target material, such as the yield strength and hardness. Therefore, it can provide a more accurate estimate of the erosion rate than simpler models that only consider a few of the impact parameters. In contrast, Finnie [11] considered the problem of sediment erosion to be a two-part problem. The first one considers a fluid mechanics analysis of the flow condition. The second part focuses on the impact angle of the particles on the target surface to calculate the volume of material removed. This angle is an essential factor in determining the erosive wear rate, as it influences how the particles interact with the material upon impact.

The erosive wear rate is not only dependent on the material's properties but also on how the impacting particles strike the surface [15]. When particles impinge at shallow angles, they tend to slide along the surface, causing less material removal [16]. On the other hand, particles impacting at steeper angles tend to dig into the material, resulting in higher erosion rates. Many industrial components such as pipes, piping accessories, turbo machinery, and injectors face erosion problems caused by suspended particles. In this sense, this study seeks to analyze the accuracy of a numerical erosion model to predict the erosion pattern for a different fluid flow from that of the original experiment, with a specific focus on turbomachinery applications in hydropower, where the presence of lithogenous sediments results in severe wear and short component life.

The analysis of this phenomenon in an open-source software environment offers an advantage in the development of more complex models and promotes a thorough and detailed study of the variables that interact in the phenomenon, as shown by Lopez [17]. His work in OpenFOAM manages to compile the model developed by Gran and Tabakoff [9], while studying the most sensitive variables of this model in a deeper level. A crucial factor addressed by the author is the omission of the fluid effects on particles during the pre-impact stage. Obtaining the contours of impact velocity, impact angle, erosion rate, and the deformation for a sand–water jet impingement on an aluminum plate surface and based

on the experimental conditions used by Nguyen, [18] the author finds that OpenFOAM provides a fully suitable environment for studying the erosion phenomenon.

Therefore, the primary goal of this study is to bridge the existing research gap by using Oka's model to describe erosion phenomena in a specific context. By exploiting the predictive capabilities of the model, this research aims to predict erosion and evaluate its temporal evolution by focusing on key parameters, namely the erosion ratio and the distribution across the plate. By considering these parameters, a better streamlined approach to assessing erosion trends over time can be developed, allowing for easier and efficient erosion analysis.

In this study, utilization of the Oka erosion model is substantiated by its well-documented advantages, as evidenced in prior research carried out by Sedrez [19] which acknowledged these merits, while Zhu [20] specifically emphasized its relevance to turbomachinery applications. One noteworthy advantage of the Oka model lies in its capacity for comprehensive parameter management, allowing for the systematic exploration of multifaceted factors influencing erosion, including the angle of impact. Moreover, the model's robustness is underscored by its extensive validation against a diverse array of experimental tests, affirming its reliability and precision. Importantly, the Oka model exhibits adaptability to material-specific characteristics, a pivotal attribute for the investigation undertaken in this study, which pertains to sand–water jet impingement on a stainless-steel surface. Ultimately, the choice to employ the Oka erosion model was guided by the overarching objective of advancing the understanding of erosion processes within the domain of hydropower applications. This endeavor seeks to yield valuable insights into the intricacies of erosion patterns and mechanisms, facilitating the optimization of materials and design strategies within this context.

To validate the proposed methodology, this study compares the erosion predictions obtained from Oka's model with the erosion patterns, also called W-shapes, derived from a previous study conducted by Nguyen [18,21]. This comparative analysis allows us to evaluate the suitability and applicability of the proposed approach in predicting erosion behavior within the given context. Furthermore, this work contributes to a better understanding of erosion phenomena while enhancing erosion management strategies.

By enhancing the knowledge of erosion processes and refining erosion prediction methodologies, this research has the potential to benefit a wide range of fields, including civil engineering, environmental science, and land management. The findings of this study will provide valuable insights into erosion dynamics and contribute to the development of more effective erosion control strategies, ultimately leading to enhanced sustainability and resilience in infrastructure and natural systems.

2. Materials and Methods

To develop this research, numerical simulations were carried out in a CFD open-source software to study the behavior of an incompressible fluid jet with inert solid particles, impacting on a solid flat surface. The focus was on the erosion rate present on the eroded surface due to the impact of these solid particles.

The numerical solution was performed using double precision to improve the computational accuracy [22]; spatial derivatives were discretized using a second-order limited centered optimized-for-vectors scheme. The Eulerian–Lagrangian approach was used to track the injected particles as a discrete phase governed by the equations of motion through the fluid domain. The continuous phase was also solved using the Navier–Stokes equations and the combined Pressure Implicit with Splitting of Operator (PISO) and Semi-Implicit Method for Pressure-Linked Equations (SIMPLE) for the pressure–velocity coupling. In addition, the k-epsilon realizable model was used to solve the turbulence phenomena. Finally, the erosion model was manually compiled in this OpenFOAM version to achieve a more robust installation of this software specifically for this case.

2.1. Liquid Phase Modeling

Fluids are treated as a continuous phase and their flow is estimated using continuity and momentum equations. The general form of the equations is as follows:

$$\frac{\partial \rho}{\partial t} + \frac{\partial (\rho u_i)}{\partial x_i} = 0 \tag{1}$$

Momentum equation:

$$\rho \frac{\partial u_i}{\partial t} + \rho \frac{\partial (u_i u_j)}{\partial x_j} = -\frac{\partial \rho}{\partial x_i} + \frac{\partial}{\partial x_j}\left[\mu\left(\frac{\partial u_i}{\partial x_j} + \frac{\partial u_j}{\partial x_i}\right)\right] + f_i \tag{2}$$

where

- u = Fluid phase velocity
- ρ = Fluid phase density
- p = Pressure
- μ = Dynamic viscosity.
- f_i = External forces.

The realizable k-ε turbulence model was selected to correctly capture the turbulent nature of the flow [23–25], which provided robustness and an improved boundary layer solving capacity under strong pressure gradients and flow separation compared to the standard k-ε model [26]. In addition, the k-ε turbulence model requires less computational effort when compared to the k-ω SST. The transport equations for the realizable k-ε take the following form:

$$\frac{\partial (\rho k)}{\partial t} + \frac{\partial (\rho k u_j)}{\partial x_j} = \frac{\partial}{\partial x_j}\left[\left(\mu + \frac{\mu_t}{\sigma_k}\right)\frac{\partial k}{\partial x_j}\right] + G_k + G_b + \rho\varepsilon - Y_M + S_k \tag{3}$$

$$\frac{\partial (\rho \varepsilon)}{\partial t} + \frac{\partial (\rho \varepsilon u_j)}{\partial x_j} = \frac{\partial}{\partial x_j}\left[\left(\mu + \frac{\mu_t}{\sigma_\varepsilon}\right)\frac{\partial \varepsilon}{\partial x_j}\right] + \rho C_1 S_\varepsilon - \rho C_2 \frac{\varepsilon^2}{k + \sqrt{\nu\varepsilon}} + C_{1\varepsilon}\frac{\varepsilon}{k} C_{3\varepsilon} G_b + S_\varepsilon \tag{4}$$

2.2. Solid Phase Modeling

The solid discrete phase was computed using a Eulerian–Lagrangian approach, where the Eulerian continuum equations were solved for water, while Newton's equations of motion were solved to capture the nature of the trajectories of the particles or group of particles. Thus, the force balance on the particle inside a viscous fluid can be written using the following equation.

$$m_P \frac{dv_P}{dt} = F_P \tag{5}$$

The term F_P can be defined as:

$$F_p = F_D + F_P + F_g + F_A \tag{6}$$

where

- F_p = Sum of forces acting over the particle,
- F_D = Drag Force for non-spherical particles,
- F_P = Pressure Gradient,
- F_g = Gravity and buoyancy force,
- F_A = Added mass or Virtual mass force.

Particle-drag models are dynamically computed based on empirical expressions for non-spherical particles.

$$F_D = \frac{3}{4}\frac{\mu_C C_D \, R_{ep}}{D + R_{ep}} \tag{7}$$

In the last expression the drag coefficient is obtained using the following equation:

$$C_D = \frac{24}{R_{ep}}\left(1 + AR_{e_p}^{B}\right) + \frac{CR_{ep}}{D + R_{ep}} \tag{8}$$

The A, B, C and D coefficient are empirical polynomial expressions that are completely explained in the study developed by Haider and Levenspiel (1989) [27]. These expressions can be written as:

$$A = \exp\left(2.3288 - 6.4581\varphi + 2.4486\varphi^2\right) \tag{9}$$

$$B = 0.0964 + 0.5565\varphi \tag{10}$$

$$C = \exp\left(4.905 - 13.8944\varphi + 18.4222\varphi^2 - 10.2599\varphi^3\right) \tag{11}$$

$$D = \exp\left(1.4681 + 12.2584\varphi - 20.7322\varphi^2 + 15.8855\varphi^3\right) \tag{12}$$

The pressure gradient force is:

$$F_P = \frac{1}{6}\pi d_p^3 \nabla P \tag{13}$$

The gravity and buoyancy force is:

$$F_g = m_p g\left(1 + \frac{\rho}{\rho_P}\right) \tag{14}$$

And the added mass force is as follows:

$$F_A = \frac{1}{12}\,\pi d_p^3 \rho_p \frac{dV_p}{dt} \tag{15}$$

Particle dispersion caused by turbulent flows can be estimated using the RAS stochastic dispersion model [28] where the velocity is perturbed in a random direction. This method, also known as the discrete random walk model, takes into account the effect of turbulent velocity fluctuations on the particle trajectories. The instantaneous fluid velocity, as shown in Equation (13), was used to integrate the particle trajectory equations along their path to predict the turbulent dispersion of particles.

Random velocity fluctuations u' were determined by Equation (14), where ζ is a Gaussian distribution random number. Particle diffusivity was estimated using Equation (15), where the integral time scale defined by Equation (16) describes the time that the particle remains in turbulent motion along a path ds.

$$u = \overline{u} + u'(t) \tag{16}$$

$$u' = \zeta\sqrt{2k/3} \tag{17}$$

$$D(t) = \overline{u_i' u_j'} T \tag{18}$$

$$T = \int_0^\infty \frac{v_p'(t) v_p'(t+s)}{\overline{v'^2}} ds \tag{19}$$

2.3. Erosion Modeling

For this case study, we employed the Oka erosion model developed by Oka and Yoshida [13,14] due to its exceptional capabilities in addressing erosion phenomena, especially in the context of liquid–solid impingement. This choice aligns with findings by Khan R [20,29] who also recognized the suitability of the Oka model for similar applications.

The Oka erosion model, as a function of the angle of impact, offers a robust framework for erosion analysis. However, it is important to note that several additional parameters are integral to the Oka model equation to ensure accurate predictions. To achieve this precision and relevance in our erosion predictions, we conducted an in-depth study outlined in the subsequent section. This study entails a meticulous process of parameter determination, which guarantees the model's efficacy in simulating erosion dynamics [17].

In the forthcoming section, we provide a comprehensive account of how these crucial parameters were derived, emphasizing the rigorous methodology employed. This meticulous approach ensures the accuracy and applicability of our erosion predictions to real-world scenarios.

Erosion Parameters

In order to estimate the erosion using the Oka model, several parameters must be known. The equation developed by Oka can be represented as:

$$E(\alpha) = g(\alpha)E_{90} \tag{20}$$

where

- α = Impact angle,
- $E(\alpha)$ = Erosion damage in $\left[\frac{\text{mm}^3}{\text{kg}}\right]$,
- $g(\alpha)$ = Impact angle dependence of the normalized erosion,
- E_{90} = Erosion damage at a normal angle.

$$g(\alpha) = (\sin(\alpha))^{n_1}(1 + Hv(1 - \sin(\alpha)))^{n_2} \tag{21}$$

$$E_{90} = K(aHv)^{k_1 b}\left(\frac{v}{v'}\right)^{k_2}\left(\frac{D}{D'}\right)^{k_3} \tag{22}$$

$$k_2 = 2.3(Hv)^{0.038} \tag{23}$$

$$n_1, n_1 = s(Hv)^q \tag{24}$$

where K is a particle property factor for the shape (angularity), a and b are model constants for the base material, v is the particle velocity, D is the particle diameter, v' is the reference particle velocity $\left(104\ \left[\frac{\text{m}}{\text{s}}\right]\right)$, and D' is the reference particle diameter $(326\ [\mu\text{m}])$. Importantly, the constants s and q are fundamental to the erosion model, and their values are contingent upon the particle material type in question. This study focuses on sediment materials typically found in Ecuadorian rivers, which exhibit a notable presence of $SiO_{2\text{-}1}$ [7]. To align our erosion model with the characteristics of these sediment types, the suggested values of s and q from Table 1 have been adopted. These values have been derived from extensive research and are tailored to suit the distinctive properties of Ecuadorian river sediments. By incorporating these coefficients into the modeling framework, the aim is to enhance the precision and applicability of erosion predictions for this specific sediment class.

Table 1. Constant exponents 's' and 'q' extracted from the study of Oka and Yoshida in 2005 [14] used as key parameters in our erosion modeling methodology.

Parameter	*s*	*q*
n_1	0.71	0.14
n_2	2.4	−0.94

The exponents k_1 and k_3 take constant values that are dependent on the type of particle used. For this case k_1 has a constant value of -0.12 and k_3 is equal to 0.19. The estimation of these values is described in detail in Oka and Yoshida [13].

Oka and Yoshida estimate the erosion rate through experimentation with several different base and particle materials. For this study, a common material for hydraulic turbine manufacturing such as SS304 stainless steel with a 196 Vickers hardness was considered.

The relatively low correlation coefficients in Figure 1 indicate a moderate degree of association between the examined parameters and erosion damage. The moderate correlations suggest that while Vickers Hardness (Hv) and Oka model parameter 'b' show some influence on erosion behavior, other factors may play significant roles as well. Erosion is a complex process influenced by numerous variables, including particle properties, impact conditions, and material characteristics, making it challenging to establish strong correlations with just a few parameters. Nevertheless, these correlations provide valuable insights into the erosion behavior of different materials, aiding in our understanding of erosion mechanisms.

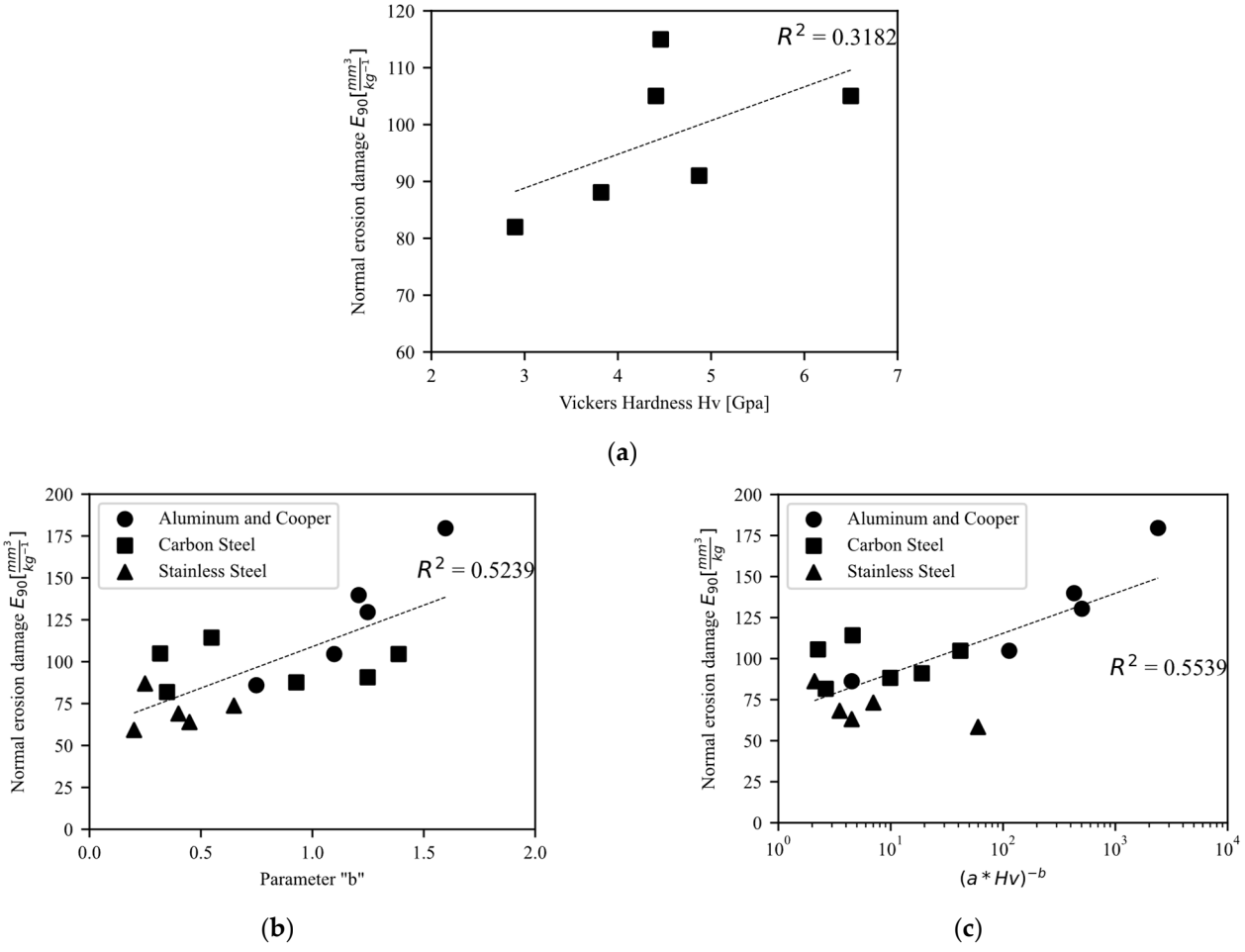

Figure 1. (**a**) Stainless steel hardness, (**b**) parameter "b", (**c**) Hv vs. E90. Graphs obtained from the investigation conducted by Oka in 2005 [13,14], illustrating key material properties relevant to our erosion modeling methodology.

The erosion rate for the material used in this work was estimated by a linear regression analysis of the experimental data and data extrapolation. Figure 1a shows the data for the relationship between the hardness of the material and the erosion damage at the normal angle E_{90}. This value corresponds to the erosion rate for 326 [µm] particles impacting at a normal angle with a velocity of 104 $\left[\frac{m}{s}\right]$. Therefore, E_{90} is determined as 82$\left[\frac{mm^3}{kg}\right]$ for the material of interest.

To calculate the value of E_{90} from Equation (22), the values of a and b were taken from Figure 1a,b and plotted from the data in Oka and Yoshida. The value of these parameters was obtained by linear regression and extrapolation. Figure 1b shows the values of the b parameter for different metallic materials and the adjusted trend line. Figure 1c shows the values of $(a \times Hv)^{-b}$ plotted against the normal erosion damage for these materials. Equation (19) can be used to calculate the erosion damage at any given velocity or particle size. However, under the controlled conditions of the experimental setup, Equation (25) is proposed to determine the erosion damage at a normal impingement angle.

$$E_{90} = K(aHv)^{-bk_1} \tag{25}$$

After estimating the adjusted values of E_{90}, a, and b for SS304, the reference erosion rate was calculated from Equation (22). The calculated values and the approximate values for the remaining parameters are shown in Table 2.

Table 2. Suggested constants for the Erosion Model extracted from Oka and Yoshida, 2005 [13,14]. These parameters are integral to configuring Oka's erosion model for our study.

Parameter	Value	Unit
K	65	-
k_1	−0.12	-
k_2	2.36	-
k_3	0.19	-
n_1	0.78	-
n_2	1.27	-
a	0.0221	-
b	0.45	-
	104	$\left[\frac{\mathrm{m}}{\mathrm{s}}\right]$
	326	$[\mu\mathrm{m}]$
Hv	1.96	[GPa]

2.4. Sediment Analysis

This study serves as a complementary analysis focused on the estimation of sediment erosion in the hydraulic turbines of the San Francisco hydro-power station in Ecuador. In order to increase understanding of the sediment characteristics, such as particle size, hardness, and shape, various tests were performed on samples collected from the Pastaza River, where the San Francisco hydro power station is located. Figure 2 shows the sieve analysis that revealed a median grain size of 9.28 [µm], indicating that the sediments are composed of fine particles. In addition, the particle density was determined to be 2650 $\left[\frac{\mathrm{kg}}{\mathrm{m}^3}\right]$, providing valuable information for the subsequent erosion analysis.

Then, to investigate the mineralogy of the sediments, X-ray diffraction was used. The results revealed a significant prevalence of plagioclase-type minerals in the sediment composition. This finding is intriguing as it differs from similar studies conducted in the Himalayan and Andean regions. Figure 3 shows a comparative diagram of the mineral composition in different regions, establishing that quartz is typically the dominant mineral found in river sediments. These contrasting results suggest that the presence of ash from the nearby Sangay volcano may have a direct impact on sediment erosion within the turbines of the hydropower station.

The identification of plagioclase-type minerals in the sediments, coupled with the influence of volcanic ash, indicates the unique geological characteristics of the study area. Further investigation of the physical and chemical properties of these minerals can provide crucial insights into the erosion processes occurring in the hydraulic turbines.

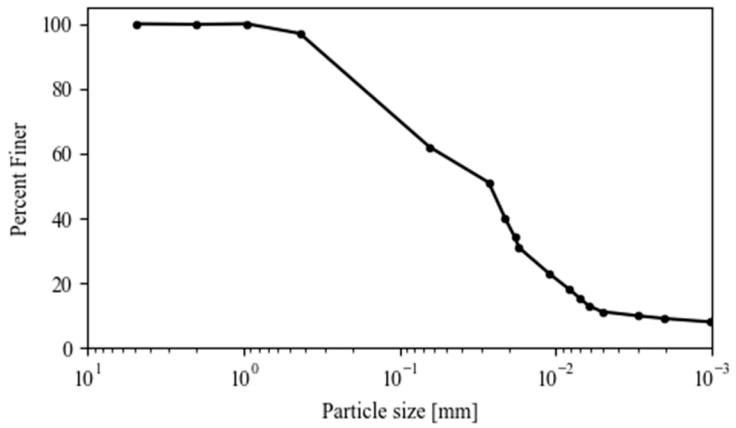

Figure 2. Results of sieve analysis on sediment samples from Ecuadorian rivers. This figure, obtained from Cruzatti's investigation [30], illustrates the size distribution of sediments found in the rivers of Ecuador, providing valuable data for our study.

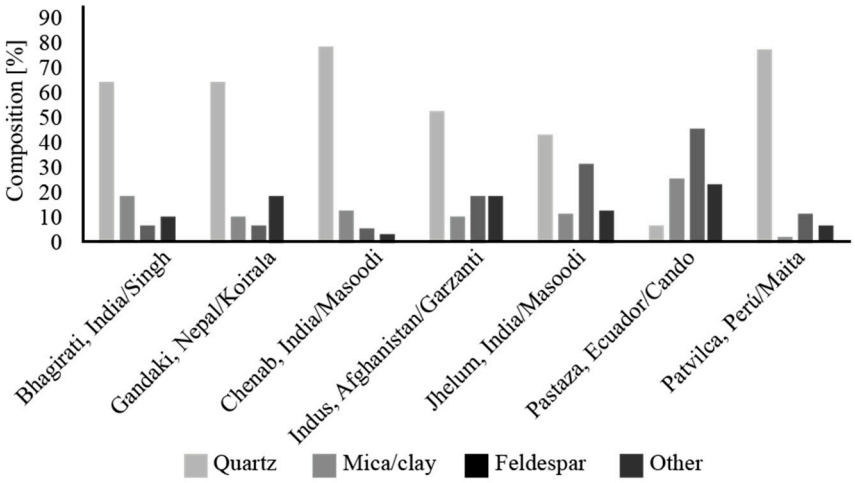

Figure 3. Comparison of sediment mineralogy across different regions. This figure offers a comparative view of sediment composition in various regions, providing insights into the differences in mineral content among these areas.

2.5. Erosion Implementation in OpenFOAM

OpenFOAM offers a versatile platform for the simulation of erosion caused by discrete solid particles, owing to its flexibility and extensibility. Users can adapt the source code to meet specific requirements, either by editing existing templates and classes or creating new ones. This level of customization enhances the adaptability of the simulation process, making it suitable for intricate studies like erosion analysis.

In this study, OpenFOAM's capabilities were employed to implement erosion modeling using the Oka et al. model [13,14,31]. Modifications were made to the "CloudFunctionObject" class to extend the functionalities of OpenFOAM solvers. These modifications enabled calculation of the discrete phase erosion, quantifying material loss resulting from the impact of solid particles on target surfaces. Specifically, a new template called "particleOKAErosion" was introduced to compile and integrate the Oka model into OpenFOAM.

In order to achieve this goal, a new template named "particleOKAErosion" was created to compile this model. This allowed for the calculation of a scalar field in cubic millimeters of eroded material ($[mm^3]$) due to the impact of discrete solid material on the studied surfaces. To achieve this purpose, the Oka model was compiled in OpenFOAM 10, which enabled the addition of the Lagrangian phase into the simulation by coupling it into

the continuous phase using the newest" clouds fvModel" functionality. This allowed for simulation of the Lagrangian phase without the need for a specific solver.

Implementation of the Oka model in OpenFOAM using C++ allowed for a more efficient and accurate simulation of the erosion caused by discrete solid particles, as demonstrated by López et al. [17,32]. By modifying the source code, the capabilities of OpenFOAM can be extended to include specific models and functionality required for the simulation process. This provides a higher level of flexibility and customization for the study of erosion mechanisms and their effects in turbomachinery.

2.5.1. Two-Way Simulation Approach

In the context of erosion analysis using OpenFOAM, the adoption of a two-way simulation approach is crucial aspect a. This approach addresses the bidirectional interaction between two distinct phases: the continuous phase (fluid) and the discrete phase (solid particles) as depicted by Oyuna [33].

In this two-way simulation, the continuous phase (fluid) dynamically influences the motion and behavior of solid particles, and conversely, the presence of solid particles impacts the fluid flow. This intricate interplay is pivotal for achieving a comprehensive understanding of erosion mechanisms. It allows for the accurate modeling of how fluid dynamics affect particle trajectories, impact angles, and material removal rates. Likewise, it captures how the presence of particles influences the fluid flow patterns, including turbulence characteristics.

2.5.2. The Significance of the Stokes Number

The Stokes number (*Stk*) is a dimensionless parameter that holds particular relevance in erosion analysis within the context of fluid–particle interaction. It quantifies the relative importance of inertia to viscous forces acting on solid particles suspended in a fluid medium [34].

$$Stk = \frac{\rho_p d_p^2 U_L}{18 \mu L_x} \tag{26}$$

where

ρ_p = Particle density,
d_p = Particle diameter,
μ = Dynamic viscosity,
L_x = Length scale,
U_L = Characteristic velocity of the fluid.

The Stokes number is calculated based on various factors, including particle size, particle density, fluid density, and the relative velocity between particles and the surrounding fluid. This parameter serves as a crucial indicator of how particles respond to fluid motion.

Specifically, a high Stokes number indicates that inertia dominates over viscous forces, implying that solid particles are less influenced by the fluid and tend to maintain their trajectories and impact angles. Conversely, a low Stokes number suggests that viscous forces are dominant, causing particles to closely follow the fluid's flow patterns and potentially leading to enhanced erosion rates [35]. In erosion simulations, considering the Stokes number is instrumental for understanding the degree of influence that fluid flow exerts on particle behavior and, consequently, erosion patterns. By assessing the Stokes number, researchers can predict how effectively particles will be transported by the fluid and how likely they are to impact and erode target surfaces.

2.6. Computational Domain

2.6.1. Geometry

This work aims to validate the calculated erosion parameters for a specific case applicable to hydropower applications by calibrating the parameters of the Oka erosion model [30]. For this purpose, the experimental setup carried out by Nguyen [18,21] was reproduced through a CFD analysis.

The aforementioned work performs an erosion evaluation of a stainless-steel commonly used in hydraulic turbines and sand particles with sizes ranging from those found in river sediments. The parameters of the experimental setup are shown in Table 3. On the other hand, the computational domain used to replicate the experiment is shown in Figure 4.

Table 3. Details of experimental setup. Sourced from Nguyen's study [18], provides valuable information for the conducted experiments.

Parameter	Value	Units
Particle velocity	30	$\left[\frac{m}{s}\right]$
Particle diameter	150	[µm]
Nozzle diameter (D)	6.4	[mm]
Particle volume fraction	0.5	[%]
Plate dimensions	$25 \times 25 \times 5$	$[mm^3]$
Standoff distance	12.7	[mm]

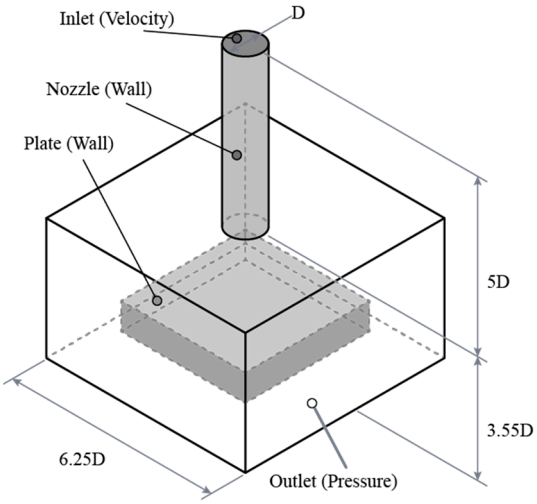

Figure 4. Computational domain and patch description. "*D*" parameter represents the diameter of the nozzle, providing a key reference for understanding the dimensions within the computational domain.

In order to ensure the reliability and accuracy of our Computational Fluid Dynamics (CFD) simulations, specific attention was paid to the convergence criteria, mesh resolution, turbulence model, and timestep.

The convergence criteria for the CFD simulations were set to ensure stability and precision. In addition, it is essential to note that the boundary conditions employed to achieve these simulations are detailed in Table 4. For the SIMPLE algorithm, which was used in the initial phase of the simulation, the residuals were required to fall below 1×10^5. Subsequently, during application of the PISO algorithm, a more stringent criterion of 1×10^4 for the residuals was employed. Additionally, the timestep for the PISO algorithm was meticulously determined as 1×10^6 seconds and held constant throughout the entire simulation. This timestep choice was motivated by the necessity to achieve a Courant number (CFL) below 1, ensuring numerical stability and preventing excessive computational diffusion.

The turbulence model employed in our simulations was the K-epsilon Realizable model, a widely accepted approach for capturing turbulent flow phenomena. To ensure the model's effectiveness, we set the turbulence intensity (k intensity) to 5%. Initial values for the turbulence kinetic energy (k) and turbulence dissipation rate (epsilon) were determined using the well-established correlations by Wilcox [36]. These initial values played a critical role in initializing the turbulence model, thereby facilitating the accurate representation of turbulent flow behavior throughout the simulation. By utilizing the K-epsilon Realizable model with carefully selected parameters, we aimed to provide a comprehensive and

reliable analysis of the erosion pattern resulting from solid particle impingement on the plate surface.

$$k = \frac{3}{2}\left(I\left|u_{ref}\right|\right)^2 \tag{27}$$

$$\epsilon = \frac{C_u^{0.75} k^{1.5}}{L} \tag{28}$$

The mesh resolution ranged from a maximum cell size of 0.316 mm to a minimum of 0.012 mm, which enabled the capture of fine-scale details of the erosion pattern. This combination of convergence criteria, timestep control, and mesh refinement enabled us to produce reliable and accurate simulation results.

Table 4. Computational Fluid Dynamics (CFD) setup. Summary of key parameters and settings for executing the erosion simulation.

Zone	Condition	Value	Units
Inlet	Velocity Inlet	30	$\left[\frac{\mathrm{m}}{\mathrm{s}}\right]$
Nozzle	Wall	No Slip	-
Plate	Wall	No Slip	-
Outlet	Pressure Outlet	0	[Pa]
Discrete Phase			
Density (ρ)	2719	$\left[\frac{\mathrm{kg}}{\mathrm{m}^3}\right]$	
Young Modulus	600	[GPa]	
Composition	SiO2-1	Silicon dioxide	

2.6.2. Computational Domain Discretization

The choice of mesh parameters is a pivotal aspect of our simulation, particularly given the use of realizable K-Epsilon turbulence models and the need for accurate particle–plate interaction modeling. To address the mesh sensitivity and ensure precise representation of the impact of particles on the plate, we carefully selected the mesh configuration.

As illustrated in Figure 5a, we incorporated 12 layers with a growth ratio of 1.2 to create a structured boundary layer mesh. This selection was made with a specific aim: achieve maximum Y+ values of up to 20 along the plate surface. These layers play a crucial role in capturing the complex turbulent behavior near the boundary and significantly contribute to the accuracy of our simulation results [37].

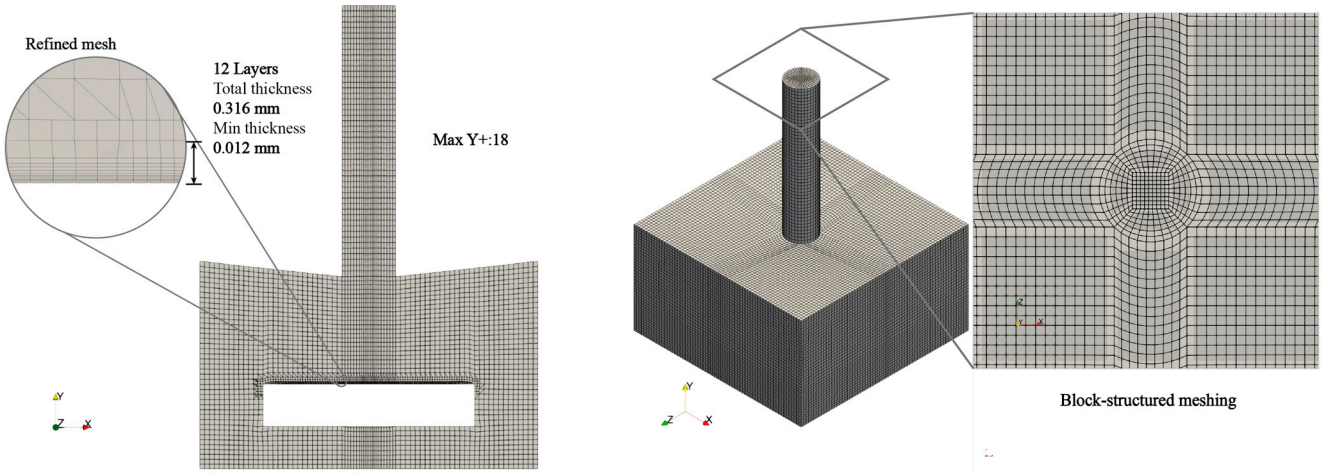

(**a**) (**b**)

Figure 5. Computational mesh and structural detail. (**a**) Slice view of the computational mesh, showcasing its intricacies. (**b**) Top view highlighting block-structured meshing details.

Our choice of 12 layers with a growth ratio of 1.2 facilitates a smooth transition from the actual element size to the refined one. This strategy ensures that the mesh accurately represents the flow dynamics and boundary layer characteristics in the vicinity of the plate, which is of paramount importance in our study of particle impact erosion.

The basis for this selection is founded on well-established principles outlined in "An Introduction to Computational Fluid Dynamics". Where, the Log-law layer, representing the turbulent region near a smooth wall, is described in detail. Beyond the viscous sublayer (where $30 < Y+ < 500$), a region exists in which both viscous and turbulent effects are significant [37,38].

By adhering to these principles and employing this mesh configuration, we aim to ensure that our simulation accurately captures the turbulent flow behavior and boundary layer dynamics, ultimately leading to reliable results in the context of particle impact erosion.

The computational domain for this study was constructed using a Block-structured meshing approach, as depicted in Figure 5b. The top view of the mesh blocks reveals the base mesh configuration achieved through the use of the open-source meshing tool called GMSH. This technique provides a systematic and controlled mesh generation process that allows for an efficient representation of the plate geometry and facilitates accurate numerical simulations.

To further refine the mesh and achieve a detailed representation of the plate, the snappyHexMesh utility was used. Based on the foundation provided by the base mesh generated by GMSH, snappyHexMesh modeled the plate geometry, resulting in a mesh with improved resolution and fidelity. The use of snappyHexMesh allowed for the capture of finer features and ensured that the mesh closely followed the contours of the plate.

The combined use of GMSH and snappyHexMesh provided a robust meshing framework for simulating particle impact on the plate surface. This approach offers the advantage of using open-source tools, enabling researchers to access and modify the meshing algorithms according to their specific needs. By employing a structured block meshing strategy and refining the mesh with snappyHexMesh, the computational model achieved a high level of accuracy and reliability in capturing the intricate physics involved in particle impact phenomena.

To select the appropriate mesh size, an independence study was conducted by systematically varying the general element size in all directions, resulting in the creation of four distinct meshes. The inlet pressure was assessed for each of these four cases, and a comprehensive analysis of convergence errors among the results was performed, as summarized in Table 5.

Table 5. Mesh independence study results. This table presents the outcomes of the mesh independence study, demonstrating the convergence of key simulation parameters with varying mesh sizes.

Nodes	Pressure (kPa)	Error (%)
299.785	66.59	1.41
496.936	67.52	1.38
770.959	68.52	1.46
1.114.943	69.12	0.88

The "Error (%)" column represents the percentage variation in pressure estimates between the different mesh configurations. It is important to note that these error values are not direct comparisons to real-world measurements but serve a specific purpose within our study. Instead, they reflect the relative differences in pressure estimates obtained from varying mesh resolutions. Specifically, the error between the pressure estimates for the 299,785 nodes mesh and the 496,936 nodes mesh was found to be less than 1.5%, a value considered acceptable for our study. Consequently, the 299,785 nodes mesh was selected for further analyses. A visual representation of the mesh employed in our CFD simulations

can be observed in Figure 5a, and additional details regarding the general characteristics of the mesh are available in Table 5.

This systematic approach ensured the selection of a mesh configuration that balances computational efficiency and accuracy, with error values serving as a critical metric to assess mesh independence and guide our choice.

2.7. Erosion Pattern Analysis

The erosion pattern analysis involved a step-by-step approach using a CFD simulation implemented in OpenFOAM. The methodology included several steps to capture the erosion behavior resulting from the impingement of solid particles on the sheet surface.

Initially, the simulation was executed using the SIMPLE algorithm (simpleFoam) without particle injection. The primary objective of this step was to calculate the pressure, velocity, turbulence kinetic energy (k), and turbulence dissipation rate (epsilon) fields until convergence was achieved. The results obtained from this initial step served as the baseline or initial conditions for subsequent stages of the simulation.

Following the initial stage, we applied the PISO algorithm (pisoFoam) while using the previously obtained results as the initial conditions. At this stage, solid particles were introduced into the flow using a custom library developed within the OpenFOAM framework, which implemented Oka's erosion model for calculation. This phase of the simulation allowed for consideration of the dynamic interaction between the solid particles and the fluid.

The simulation was allowed to run until a new pseudo-stabilization stage was reached, which occurred at approximately 0.2 s into the simulation. During this pseudo-stabilization stage, no additional external interactions or disturbances were introduced into the system. The primary objective of this stage was to observe the erosion pattern resulting from the impingement of solid particles on the plate surface. It was during this phase that we gained valuable insights into the spatial distribution and characteristics of the erosion pattern.

It is important to note that throughout the simulation, a time step of 1×10^{-6} s was employed to ensure accurate tracking of the dynamic interactions between particles and the fluid. The decision to continue the simulation until approximately 0.2 s allowed us to observe the erosion pattern under quasi-steady-state conditions.

Subsequently, a detailed analysis of the erosion pattern was conducted. It was observed that the erosion pattern exhibited minimal changes before reaching the stabilization point at around 0.2 s of simulated time. Additionally, the erosion rate over the entire plate surface reached a relatively stable value at this point. Based on these observations and to simplify the simulation, the assumption that the erosion pattern would remain relatively consistent beyond the stabilization point was made. This decision allowed us to focus on studying the long-term erosion behavior resulting from prolonged solid particle impingement on the plate surface.

By following this methodological approach, we effectively analyzed the erosion pattern resulting from the impingement of solid particles on the plate surface. This approach provided us with a comprehensive understanding of the erosion behavior and its long-term effects, offering valuable insights for the development of erosion control and management strategies.

3. Results

3.1. Liquid–Solid Phase Results

The velocity and pressure fields from the flow calculation are shown in Figure 5a,b. A stagnation point is seen in the zone just below the center of the impingement jet, where the velocity of the flow is zero due to the high pressure in the area where the water flow is diverted. This high-pressure region is caused by deceleration and deflection of the flow velocity as it impinges on the surface of the material, resulting in progressive upstream deceleration [39,40]. Therefore, a lower erosion rate is expected below this region, where material removal may be mainly caused by recirculating particles.

Figure 6 shows the trajectory and velocity of solid particles contrasted with a flow velocity contour. The difference between the velocity of the particles and that of the flow is negligible.

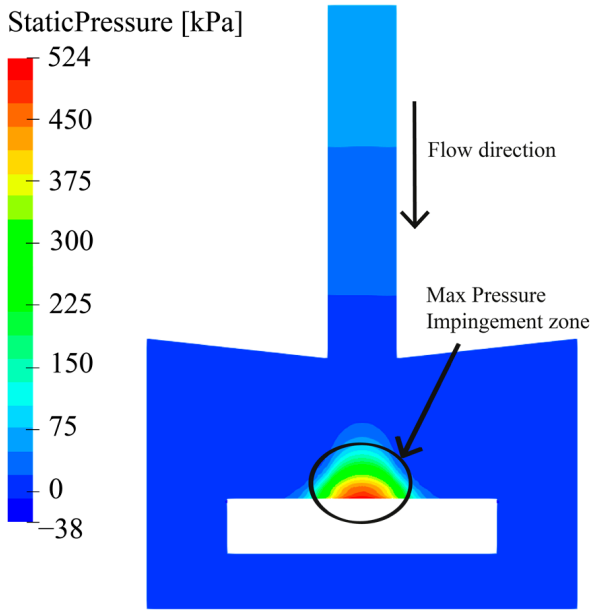

Figure 6. Pressure field.

The equilibrium between the particles and the carrier fluid depends directly on the Stokes number, e.g., when the Stokes number is much less small than one, the particle can maintain near velocity equilibrium with the continuous phase. Moreover, when the Stoke number is larger than one, the particle motion is non-affected by the carrier flow field [22]. When calculating the Stokes number of the particles in this study, this becomes obvious since Stk = 0.0236 and less than 0.1, which means that the particles are expected to closely follow the water streamlines.

The relationship between particle trajectories and fluid streamlines was investigated in this study using the computational fluid dynamics software OpenFOAM and post-processing in Paraview. As depicted in Figure 7b,c, the particles behavior was accurately captured in this software, demonstrating a close relationship between particle trajectories and fluid streamlines. The expected correlation between them was observed, indicating that the particles followed the general flow patterns established by the fluid.

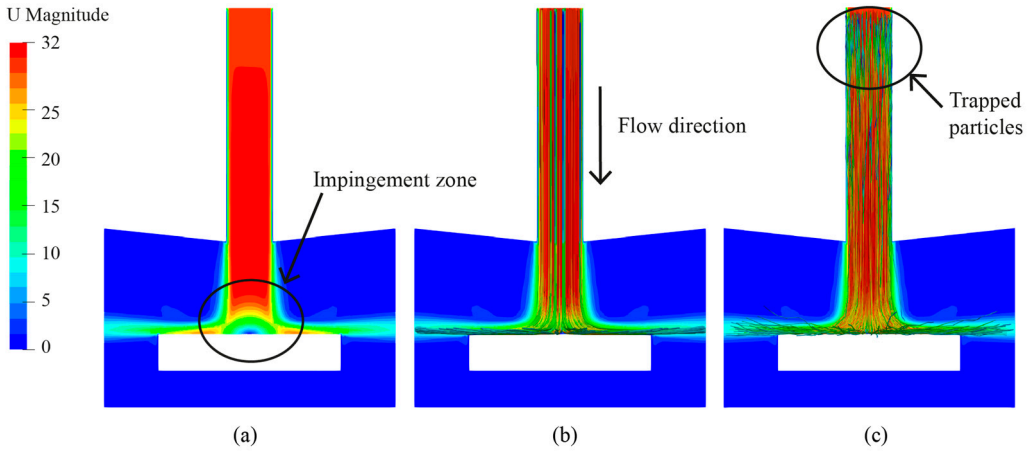

Figure 7. Velocity field (**a**), liquid streamlines (**b**), and particle trajectory (**c**).

However, there is a difference at the inlet, where particles can become trapped and flow at a lower velocity due to the non-slip condition on the walls.

Figure 7c shows the streamlines of the fluid carrier, revealing slight differences compared to the particle trajectories. A notable difference is observed at the inlet walls, where some particles are trapped by the no-slip condition, leading to a significant decrease in their velocity. However, as the particle distribution moves away from the zero-velocity region, they exhibit the same behavior as the surrounding fluid.

Another notable difference is the bouncing motion of the particles just before impact. Although the particles experience a change in velocity after each bounce, they are effectively carried by the fluid due to the considerably higher fluid velocity. As a result, the overall behavior of the particles aligns with that of the fluid streamlines.

By closely examining the relationship between particle trajectories and fluid streamlines, this study provides valuable insights into the dynamics of particle–fluid interaction.

3.2. Erosion Results

As described in the methodology section, the simulation reached a pseudo-stable state at approximately 0.2 s. Figure 8 show the average stabilization of the erosion rate over time, indicating that the erosion rate reached a stable value at this point. Specifically, the erosion rate was determined to be 3.5×10^{-4} mm^3.

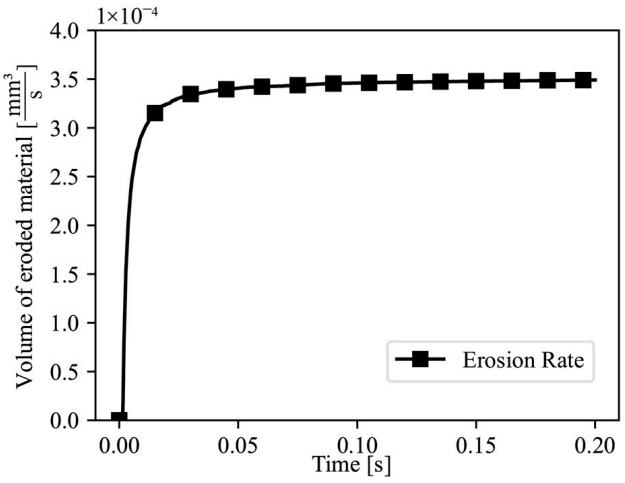

Figure 8. Erosion ratio mean of the plate's surface.

Once a stabilized erosion rate at 0.2 s had been achieved, the next step was to determine the pattern of erosion and to approximate the depth of erosion associated with that pattern. This depth of erosion would then be used for a comparative analysis with the experimental data. To validate this study, the surface removal material due to erosion was analyzed for different impingement times and compared to that of the experimental evaluation in Nguyen [18], as seen in Figure 9. The comparison would focus on the depth of erosion across the plate surface, as shown in Figure 7a. To evaluate the depth of erosion over the plate surface, the erosion ratio ([mm^3]), was divided by the area of the corresponding surface ($[\mathrm{mm}^2]$), which includes the region where the erosion value was obtained, as shown in Figure 9a.

By dividing the erosion ratio by the surface area, a quantitative assessment of the depth of erosion was obtained. This parameter was used to characterize the extent of material removal due to erosion. Comparison of the calculated depth of erosion with the experimental data from Nguyen et al. [18] would provide insight into the accuracy and reliability of the simulation in replicating real-world erosion patterns.

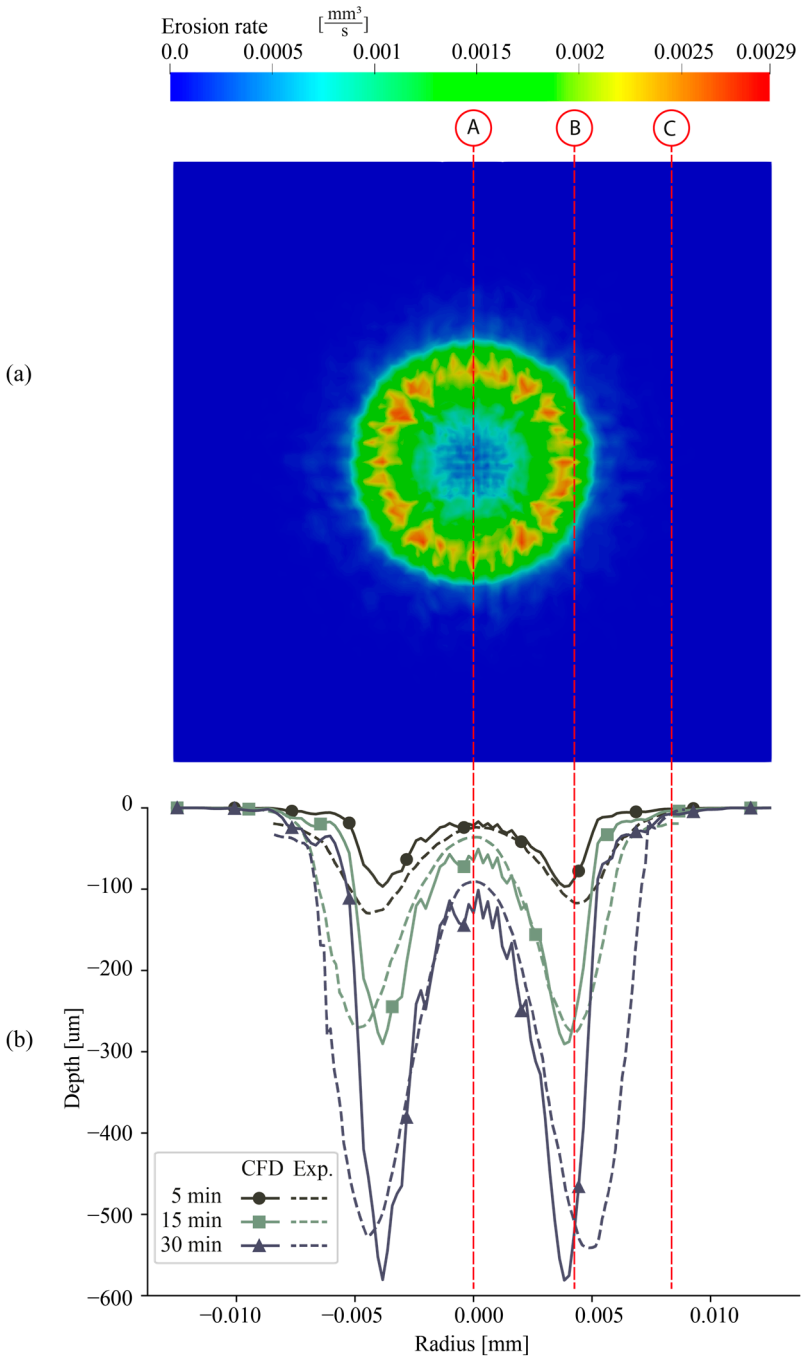

Figure 9. (**a**) Erosion ring over surface plate, (**b**) "W-Shape" of the simulation and the experiment.

Figure 7c displays the erosion pattern obtained by discrete phase analysis at 90; the expected "W" shape in the erosion pattern is attributed to the presence of a high-pressure zone, as described in the previous section. The flow velocity outside the stagnation zone changes direction while maintaining a high velocity. Consequently, the region adjacent to the stagnation point was expected to exhibit high erosion rates. The annular zone, located between 4 and 6 mm from the center of the plate, corresponds approximately to the distance from the stagnation point where the flow velocity remains high, and the particles initially impact the stainless-steel plate. Peak erosion values occurred in this annular zone.

In Figure 8, a notable observation emerges in the absence of external influences on water impingement—a state of pseudo-stability. Here, a consistent erosion rate prevailed over time, indicating uniform detachment of the eroded volume across the surface. This

discovery highlights the erosion process's potential to achieve remarkable stability under specific conditions, bearing implications for diverse applications.

To validate the erosion patterns, particular attention was given to the central, peak, and edge regions of the erosion ring, as depicted in Figure 9, which are considered the primary points of interest. Table 6 presents the corresponding depth values in micrometers (μm) obtained from the CFD simulations conducted in this study. These numerical results were assessed and compared to the depth measurements obtained from the experimental study conducted by Nguyen in 2014 [18], specifically at the same central, peak, and edge regions.

Table 6. Depth of the interest points CFD.

Time	Depth (μm)		
	Center	**Peak**	**Border**
5 min	-24.3 ± 2.1	-95.6 ± 5.3	-5 ± 1.2
15 min	-50.6 ± 3.8	-291.0 ± 7.2	-21 ± 2.5
30 min	-91 ± 4.5	-580.5 ± 8.7	-37 ± 3.1

By comparing these depth values, a comprehensive evaluation of the erosion patterns was achieved, facilitating a quantitative comparison between the simulation and experimental results. This approach allowed us to validate the accuracy of our numerical model by directly aligning it with the experimental findings from Nguyen's study, which investigated the effect of surface evolution on water–sand multiphase flow characteristics and material erosion behavior.

As expected, the center point exhibited less erosion depth. This behavior can be attributed to the high pressure experienced at this location, causing the particles deceleration and a lower erosion ratio. In contrast, the peak region showed the highest amount of material erosion. This phenomenon can be explained by the acceleration experienced by the particles due to the pressure field and the impact angle with the plate. Lastly, the boundary region displayed relatively low erosion depths and gradually approached zero, indicating minimal or no erosion at the surface.

The comparison between the experimental data and the results obtained from the CFD simulation allowed us to analyze the agreement or discrepancy of the erosion depths. Tables 6 and 7 show the depth values at different time intervals for the center, peak, and border regions of interest.

Table 7. Depth of the interest points [18].

Time	Depth (μm)		
	Center	**Peak**	**Border**
5 min	−22.5	−116.2	−14.3
15 min	−46.6	−280.3	−16.8
30 min	−101.3	−541.5	−27.1

Analyzing the results, it was observed that the CFD simulation and experimental study generally agree. In terms of the central region, the CFD simulation shows erosion depths ranging in micrometers from −22.5 to −101.3, while the experimental depths range from −24.3 to −91. This indicates a relatively close agreement, with the CFD simulation slightly underpredicting the erosion depths compared to the experimental measurements. The observed differences can be attributed to several factors, including uncertainties in the boundary conditions and the simplifications made in the simulation setup.

Moving to the peak region, the CFD simulation yields erosion depths ranging in micrometers from −95.6 to −580.5, while the experimental depths range from −116.2 to −541.5. Here, we see a similar trend, with the CFD simulation generally underpredicting the erosion depths compared to the experimental data. The peak region was characterized

by more significant erosion, which can be attributed to the acceleration effects caused by the pressure field and the impact angle of the particles. The inherent complexity of accurately capturing these effects in the simulation may explain the slight discrepancies between the simulation and experimental results.

For the border region, both the CFD simulation and the experimental data show relatively low erosion depths ranging in micrometers from −5 to −37 and from −13.4 to −27.1, respectively. The erosion in this region is minimal compared to the center and peak regions, indicating that the impact of the particles near the edge is less significant. The agreement between the CFD simulation and experimental measurements in this region suggests that the simulation accurately captures the overall erosion pattern.

Figure 9 presents a set of three sub-plots, each depicting the W-shape erosion pattern at different time intervals (5, 15, and 30 min). The comparison between the experimental data and the simulated results shows a high degree of accuracy in capturing the erosion behavior.

The comparative analysis of erosion depths between the CFD simulation and the experimental data from Nguyen et al. [18] reveals a generally reasonable agreement in the central, peak, and border regions over different time intervals. Minor variations exist, with the simulation slightly overestimating erosion depths in the central and peak regions by up to approximately 8.89% and slightly underestimating depths by up to about 8.03%, respectively. However, in the border region, both the simulation and experimental measurements closely match, with differences of less than 2% at all time intervals. These findings collectively suggest that the CFD simulation provides a reliable representation of erosion behavior over time, with variations well within an acceptable range. This validation underscores the effectiveness of the simulation in replicating real-world erosion patterns in hydro-power applications, offering valuable insights into erosion dynamics and aiding in engineering decision making and material selection for erosion-resistant components.

At the initial time of 5 min, the W-shape pattern obtained from the experiment closely matched with the simulated data. The erosion depths at the center, peak, and border regions exhibit good agreement, indicating the reliability of the simulation model. This agreement further validates the methodology used in this study.

As the impingement time extended to 15 and 30 min, slight deviations were observed between the experiment and the simulation. These deviations can be attributed to the physical material removal that occurs in the experiment but is not considered in the CFD simulation. The experimental setup can introduce additional factors such as particle accumulation, changes in the impact angle, or surface roughness that can affect the erosion behavior. Despite these minor discrepancies, the overall trend of the W-shape pattern remains consistent between the experiment and the simulation. This suggests that the simulation accurately captured the primary mechanisms responsible for erosion, such as the high-pressure zones and the impact of particles on the plate surface.

4. Discussion

This study unveils the successful application of transient state analyses in predicting erosion behavior in scenarios characterized by low material loss rates and short impingement times, where material loss minimally impacts flow dynamics. This finding highlights the potential of Computational Fluid Dynamics (CFD) simulations for gaining insights into erosion behavior, particularly in situations where conducting physical experiments presents challenges.

The implementation of Oka's erosion model within the OpenFOAM framework plays a pivotal role in this research. Oka's model integrates crucial parameters and formulations to describe the erosion process, primarily driven by the impact of solid particles on surfaces. This model incorporates various factors, encompassing particle size, impact velocity, and surface characteristics, enabling accurate predictions of erosion rates.

In a similar manner, Nguyen's study employed a comparable methodology, acknowledging the influence of mass loss on plate deformation. Nguyen's approach involved employing various meshes with pre-affected surface plates to validate thickness variation

over time; although this method is comprehensive, it comes with substantial computational demands [18].

In contrast, this study introduces a streamlined approach for assessing surface deformation. By leveraging Oka's model and the concept of pseudo-stabilization of erosion rates, a lightweight methodology was developed. This approach allows us to approximate changes in surface profiles within shorter timeframes, albeit with some limitations in representing extended periods of impingement. While this approach offers computational advantages, exploring potential refinements or extensions to Oka's model could address observed discrepancies in erosion depth predictions.

Comparing the experimental data with simulation results generally reveals favorable agreement, particularly concerning the center and border regions of the erosion ring. Minor disparities stem from uncertainties related to boundary conditions and simplifications within the simulation setup. Nonetheless, the slight underestimation of erosion depths in the central and peak regions suggests the potential for enhancing the simulation model.

This study, while offering valuable insights into erosion modeling and analysis, acknowledges inherent limitations. Notably, a simplified approach was employed to simulate particle–wall interactions due to practical considerations and computational constraints. Modeling individual solid particles' intricate interactions with the wall surface, including their impact on surface deformation and erosion, can be computationally demanding. Implementing such a detailed approach could render simulations prohibitively expensive, particularly for longer durations or more complex geometries.

Contrasting with prior work, Lopez's study introduced a complex methodology within the OpenFOAM framework to capture surface deformation caused by particle impingement [32]. However, Lopez's approach did not account for variations in surface plate material. In contrast, this study aimed to address this limitation by implementing a more robust erosion model that considers the material characteristics of the surface plate. Importantly, this was achieved with fewer computational resources, making this approach a pragmatic alternative where both accuracy and computational efficiency are paramount.

Nonetheless, a significant limitation must be acknowledged—the exclusion of physical material removal in the simulations. This omission could affect the precision of erosion depth predictions, particularly in cases involving longer impingement durations. Future research endeavors should explore incorporating material removal effects to provide a more comprehensive understanding of erosion behavior.

This study underscores the significance of understanding the interaction between fluid and solid phases, a critical aspect influencing particle trajectories and impact angles, thereby significantly shaping erosion rates. In prior research, Nguyen's study conducted a rigorous analysis of particle dispersion within a fluid domain, inspiring aspects of this study [18,21]. However, this study opted for the K-epsilon realizable turbulence model, given its established utility in turbomachinery applications, as evidenced in Cruzzati's work [22,30]. It is pertinent to note that while this approach has proven successful in certain contexts, further scrutiny and adjustments may be required to ensure its compatibility with all scenarios, including those involving particle-laden flows near surfaces.

Regarding the quoted scenarios, there is a wide variety of materials and coating deposition techniques in renewable energy applications that will benefit from simulation [1–6]. Therefore, numerical modeling of erosion (which is a common wear mechanism in these applications) provides a practical understanding of the base material–particle interactions prior to the experimental phase under coating conditions. This facilitates the selection of the most suitable coating for an application, considering factors such as hardness, roughness, and abrasion resistance. This study's implications extend well beyond the hydropower sector. It holds promise for various industries, including renewable energy, where it can aid in fortifying wind turbine blade designs and maintenance to resist erosion from airborne particles. Industries such as oil and gas can apply these insights to enhance material selection and maintenance practices for materials regularly exposed to abrasive substances in pipelines and equipment. Furthermore, this research can inform the

development of erosion-resistant coatings for aircraft surfaces, while in the solar energy field, the methodology can be adapted to improve coatings' erosion resistance. Recent studies [7,8] have highlighted the potential for optimizing coatings for solar panels using innovative approaches like Zr-oxide doping.

This paper successfully presents a robust numerical analysis of erosion modeling in liquid–solid impingement. The results contribute to the understanding of erosion processes and highlight the potential of CFD simulations in erosion modeling and analysis. By comparing simulation results with experimental data, the paper demonstrates the reliability and accuracy of the proposed methodology. However, future studies should address the limitations and explore ways to further improve the simulation accuracy to achieve even more accurate predictions of erosion phenomena, including potential refinements to Oka's erosion model.

Prospective investigations may delve into dynamic mesh evolution predicated on material removal rates and real-time solver-run mesh updates. While necessitating substantial computational resources, such advancements hold promise for enhancing the precision of predictions pertaining to the studied phenomena.

5. Conclusions

The analysis yields an average error of approximately 5.12% between the computational fluid dynamics (CFD) simulation and the real-world experimental data for erosion depths in the center and peak regions at various time intervals. This modest level of error underscores the overall reliability and validation of the CFD simulation in replicating real-world erosion patterns.

The study successfully reached a pseudo-stable state in the erosion rate at approximately 0.2 s, with an erosion rate quantified at 3.5×10^{-4} mm^3. This achievement allowed for a quantitative assessment of erosion depth and pattern, serving as a basis for comparative analysis with experimental data. This pseudo-stabilization provides a critical reference point for understanding the temporal dynamics of erosion in hydro-power applications.

The developed CFD simulation encompasses methodology, erosion rate calculations, point-wise comparisons, and W-shaped erosion pattern evaluations, providing a dependable and precise depiction of the erosion process. The close agreement between experimental and simulated data further validates the effectiveness of the proposed methodology in elucidating erosion phenomena. Despite minor discrepancies, the overall agreement between the simulation and experimental measurements is reasonable. In the central region, the simulation tends to slightly overestimate erosion depths by approximately 6.24%. In the peak region, it slightly underestimates depths by about 2.79%. These variations, while present, fall within an acceptable range and affirm the practical utility of the CFD simulation in assessing erosion dynamics.

It is imperative to recognize the inherent limitations of this simulation, especially the absence of physical material removal considerations. This limitation warrants careful interpretation of the results. Nonetheless, the simulation remains an invaluable tool for comprehending and predicting erosion behavior, particularly in situations where conducting physical experiments poses challenges or consumes excessive time. Once the limitations are overcome, the research can lead to the implementation of coatings within this numerical proposal.

Author Contributions: Conceptualization, C.C., X.L., G.A. and E.C.; Data curation, M.N. and C.C.; Investigation, M.N., C.C., J.E. and E.C.; Methodology, M.N., C.C., V.H., J.E. and G.A.; Project administration, E.C.; Resources, E.C.; Software, M.N. and V.H.; Supervision, E.V., V.H., A.T., G.A. and E.C.; Validation, M.N., C.C. and J.E.; Visualization, X.L., A.T. and E.C.; Writing—Original draft, M.N.; Writing—Review and editing, M.N., E.V., A.T. and J.E. All authors have read and agreed to the published version of the manuscript.

Funding: This research was funded by "Corporación Ecuatoriana para el Desarrollo de la Investigación y la Academia (CEDIA)" and the Escuela Politécnica Nacional (PIEX-CEDIA-XVII-2022-77). This research was funded by Escuela Politécnica Nacional (PIS 19-06).

Institutional Review Board Statement: Not applicable.

Informed Consent Statement: Not applicable.

Data Availability Statement: The data presented in this study are available on request from the corresponding author. The data are not publicly available due to contractual obligations with collaborating organizations.

Acknowledgments: The authors would like to thank to Corporación Ecuatoriana para el Desarrollo de la Investigación y la Academia (CEDIA) for the financial support given to the present research, development, and innovation work through its program, especially for the I+D+i found for the Project PIEX-CEDIA-XVII-2022-77.

Conflicts of Interest: The authors declare no conflict of interest.

References

1. Anurag Kumar, N.; Mishra, S. Slurry erosion: An overview. *Mater Today Proc.* **2019**, *25*, 659–663. [CrossRef]
2. Nath, G.; Kumar, S. Slurry Erosion Behaviour of Pack Boronized 13-4 Martensitic Stainless Steel for Hydro Turbine Blades. *Mater Today Proc.* **2018**, *5*, 17380–17388. [CrossRef]
3. Mahajan, D.; Tajane, R. A Review on Ball Burnishing Process. *Int. J. Sci. Res. Publ.* **2013**, *3*, 1–8.
4. Goyal, D.K.; Singh, H.; Kumar, H. Characterization and Accelerated Erosion Testing of WC-Co-Cr- and CoNiCrAlY-Coated CA6NM Turbine Steel. *J. Therm. Spray Technol.* **2019**, *28*, 1363–1378. [CrossRef]
5. Hadad, M.; Hitzek, R.; Buergler, P.; Rohr, L.; Siegmann, S. Wear performance of sandwich structured WC-Co-Cr thermally sprayed coatings using different intermediate layers. *Wear* **2007**, *263*, 691–699. [CrossRef]
6. Prashar, G.; Vasudev, H.; Thakur, L. Performance of different coating materials against slurry erosion failure in hydrodynamic turbines: A review. *Eng. Fail Anal.* **2020**, *115*, 104622. [CrossRef]
7. Zambrano-Mera, D.F.; Espinoza-González, R.; Villarroel, R.; Rosenkranz, A.; Carvajal, N.; Pintor-Monroy, M.I.; Montaño-Figueroa, A.G.; Arellano-Jiménez, M.J.; Quevedo-López, M.; Valenzuela, P.; et al. Optical and mechanical properties of Zr-oxide doped TiO_2/SiO_2 anti-reflective coatings for PV glass covers. *Sol. Energy Mater. Sol. Cells* **2022**, *243*, 111784. [CrossRef]
8. Zambrano-Mera, D.F.; Espinoza-González, R.; Rosenkranz, A.; Harvey, T.J.; Polcar, T.; Valenzuela, P.; Gacitúa, W. Enhanced erosion resistance of anti-reflective TiO_2/SiO_2 coatings induced by Zr-oxide doping. *Sol. Energy Mater. Sol. Cells* **2023**, *250*, 112079. [CrossRef]
9. Grant, G.; Tabakoff, W. *An Experimental Investigation of the Erosive Characteristics of 2024 Aluminum Alloy*; Department of Aerospace Engineering, University of Cincinnati: Cincinnati, OH, USA, 1973.
10. Bitter, J.G.A. A Study of erosion phenomena: Part I. *Wear* **1963**, *6*, 169–190. [CrossRef]
11. Finne, I. Erosion of surfaces. *Wear* **1960**, *3*, 87–103. [CrossRef]
12. Arabnejad, H.; Mansouri, A.; Shirazi, S.A.; McLaury, B.S. Development of mechanistic erosion equation for solid particles. *Wear* **2015**, *332–333*, 1044–1050. [CrossRef]
13. Oka, Y.I.; Yoshida, T. Practical estimation of erosion damage caused by solid particle impact: Part 2: Mechanical properties of materials directly associated with erosion damage. *Wear* **2005**, *259*, 102–109. [CrossRef]
14. Oka, Y.I.; Okamura, K.; Yoshida, T. Practical estimation of erosion damage caused by solid particle impact: Part 1: Effects of impact parameters on a predictive equation. *Wear* **2005**, *259*, 95–101. [CrossRef]
15. Khan, M.R.; Ya, H.H.; Pao, W.; Majid, M.A.A. Numerical Investigation of Sand Particle Erosion in Long Radius Elbow for Multiphase Flow. In *Advances in Material Sciences and Engineering*; Springer: Singapore, 2020; pp. 41–49.
16. Abduljabbar, A.; Mohyaldinn, M.E.; Younis, O.; Alghurabi, A.; Alakbari, F.S. Erosion of sand screens by solid particles: A review of experimental investigations. *J. Pet. Explor. Prod. Technol.* **2022**, *12*, 2329–2345. [CrossRef]
17. López, A.; Stickland, M.T.; Dempster, W.M. CFD study of fluid flow changes with erosion. *Comput. Phys. Commun.* **2018**, *227*, 27–41. [CrossRef]
18. Nguyen, V.B.; Nguyen, Q.B.; Liu, Z.G.; Wan, S.; Lim, C.Y.H.; Zhang, Y.W. A combined numerical-experimental study on the effect of surface evolution on the water-sand multiphase flow characteristics and the material erosion behavior. *Wear* **2014**, *319*, 96–109. [CrossRef]
19. Sedrez, T.A.; Decker, R.K.; da Silva, M.K.; Noriler, D.; Meier, H.F. Experiments and CFD-based erosion modeling for gas-solids flow in cyclones. *Powder Technol.* **2017**, *311*, 120–131. [CrossRef]
20. Zhu, H.; Zhu, J.; Rutter, R.; Zhang, J.; Zhang, H.Q. Sand erosion model prediction, selection and comparison for electrical submersible pump (ESP) using CFD method. In *Fluids Engineering Division Summer Meeting*; American Society of Mechanical Engineers, Fluids Engineering Division (Publication) FEDSM: Quebec, QC, Canada, 2018; Volume 3, pp. 1–10.

21. Nguyen, V.B.; Nguyen, Q.B.; Zhang, Y.W.; Lim, C.Y.H.; Khoo, B.C. Effect of particle size on erosion characteristics. *Wear* **2016**, *348–349*, 126–137. [CrossRef]
22. Cando, E.; Yu, A.; Zhu, L.; Liu, J.; Lu, L.; Hidalgo, V.; Luo, X.W. Unsteady numerical analysis of the liquid-solid two-phase flow around a step using Eulerian-Lagrangian and the filter-based RANS method. *J. Mech. Sci. Technol.* **2017**, *31*, 2781–2790. [CrossRef]
23. Iovaănel, R.G.; Bucur, D.M.; Cervantes, M.J. Study on the accuracy of RANS modelling of the turbulent flow developed in a Kaplan turbine operated at, B.E.P. Part 1—Velocity field. *J. Appl. Fluid Mech.* **2019**, *12*, 1449–1461.
24. Liu, H.L.; Liu, M.M.; Dong, L.; Ren, Y.; Du, H. Effects of computational grids and turbulence models on numerical simulation of centrifugal pump with CFD. *IOP Conf. Ser. Earth Environ. Sci.* **2012**, *15*, 062005. [CrossRef]
25. Stoessel, L.; Nilsson, H. Steady and unsteady numerical simulations of the flow in the Tokke Francis turbine model, at three operating conditions. *J. Phys. Conf. Ser.* **2015**, *579*, 012011. [CrossRef]
26. Cando, E.H.; Luo, X.W.; Hidalgo, V.H.; Zhu, L.; Aguinaga, A.G. Experimental study of liquid-solid two phase flow over a step using PIV. *IOP Conf. Ser. Mater. Sci. Eng.* **2016**, *129*, 012054. [CrossRef]
27. Haider, A. Drag Coefficient and Terminal Velocity of Spherical and Nonspherical Particles. *Powder Technol.* **1989**, *58*, 63–70. [CrossRef]
28. Greenshields, C. *OpenFOAM v11 User Guide*; The OpenFOAM Foundation: London, UK, 2023; Available online: https://doc.cfd.direct/openfoam/user-guide-v11 (accessed on 24 October 2023).
29. Khan, R.; Ya, H.H.; Pao, W. Numerical investigation of the influence of sand particle concentration on long radius elbow erosion for liquid-solid flow. *Int. J. Eng. Trans. A Basics* **2019**, *32*, 1485–1490.
30. Cruzatty, C.; Jimenez, D.; Valencia, E.; Zambrano, I.; Mora, C.; Luo, X.; Cando, E. A case study: Sediment erosion in francis turbines operated at the san francisco hydropower plant in ecuador. *Energies* **2022**, *15*, 8. [CrossRef]
31. Oka, Y.I.; Ohnogi, H.; Hosokawa, T.; Matsumura, M. The impact angle dependence of erosion damage caused by solid particle impact. *Wear* **1997**, *203–204*, 573–579. [CrossRef]
32. López, A.; Nicholls, W.; Stickland, M.T.; Dempster, W.M. CFD study of Jet Impingement Test erosion using Ansys Fluent®and OpenFOAM®. *Comput. Phys. Commun.* **2015**, *197*, 88–95. [CrossRef]
33. Rybdylova, O.; Zaripov, T.; Li, Y. Two-way coupling of the fully Lagrangian Approach with OpenFOAM for spray modelling. *Proc. ILASS* **2019**, *2019*, 244256.
34. Pouraria, H.; Darihaki, F.; Park, K.H.; Shirazi, S.A.; Seo, Y. CFD modelling of the influence of particle loading on erosion using dense discrete particle model. *Wear* **2020**, *460–461*, 203450. [CrossRef]
35. Pour, H.R.Z.; Iovieno, M. The Effect of Particle Collisions on Heat Transfer in a non-Isothermal Dilute Turbulent Gas-Particle Flow. In Proceedings of the 8th World Congress on Momentum, Heat and Mass Transfer, Portugal, Lisbon, 26 March 2023; pp. 1–8.
36. Wilcox, D.C. *Turbulence Modeling for CFD*, 3rd ed.; DCW Industries, Inc.: La Cañada, CA, USA, 2006; Available online: http://www.dcwindustries.com (accessed on 24 October 2023).
37. Puga, D.; Escaler, X.; Hidalgo, V.; Luo, X. Mesh dependence analysis for simulating unsteady cavitation around a plane convex hydrofoil. *IOP Conf. Ser. Earth Environ. Sci.* **2022**, *1079*, 012043. [CrossRef]
38. Versteeg, H.K.; Malalasekera, W. *An Introduction to Computational Fluid Dynamics*, 2nd ed.; Pearson Education Ltd.: Harlow, UK, 2007.
39. Fitzgerald, J.A.; Garimella, S.V. *Visualization of the Flow Field in a Confined and Submerged Impinging Jet*; American Society of Mechanical Engineers, Heat Transfer Division (Publication) HTD: New York, NY, USA, 1997; Volume 346, pp. 93–96.
40. Lee, J.L. Stagnation region heat transfer of a turbulent axisymmetric jet impingement. *Exp. Heat Transf.* **1999**, *12*, 137–156. [CrossRef]